

# Enhancing Reinforcement Learning for Radiology Report Generation with Evidence-aware Rewards and Self-correcting Preference Learning

Anonymous ACL submission

## Abstract

Recent reinforcement learning (RL) approaches have advanced radiology report generation (RRG), yet two core limitations persist: (1) report-level rewards offer limited evidence-grounded guidance for clinical faithfulness; and (2) current methods lack an explicit self-improving mechanism to align with clinical preference. We introduce clinically aligned Evidence-aware Self-Correcting Reinforcement Learning (ESC-RL), comprising two key components. First, a Group-wise Evidence-aware Alignment Reward (GEAR) delivers group-wise, evidence-aware feedback. GEAR reinforces consistent grounding for true positives, recovers missed findings for false negatives, and suppresses unsupported content for false positives. Second, a Self-correcting Preference Learning (SPL) strategy automatically constructs a reliable, disease-aware preference dataset from multiple noisy observations and leverages an LLM to synthesize refined reports without human supervision. ESC-RL promotes clinically faithful, disease-aligned reward and supports continual self-improvement during training. Extensive experiments on two public chest X-ray datasets demonstrate consistent gains and state-of-the-art performance.

## 1 Introduction

Radiology reports translate medical images into clinical knowledge, enabling efficient interpretation and decision-making. Yet producing high-quality reports demands careful attention to subtle visual cues and precise medical terminology, making it time-consuming and cognitively intensive. As imaging volumes surge, automated radiology report generation offers a promising path to reduce radiologists' workload.

Current RRG approaches have achieved remarkable progress by incorporating knowledge graphs (Yin et al., 2025), contrastive learning (Li et al., 2024), retrieval augmentation (Zhou et al., 2025b),

and large language models (LLMs) (Hou et al., 2025; Zhang et al., 2025). Recently, Reinforcement learning (RL) has gained traction for its strong empirical performance in gameplay, robotics, autonomous systems, and multimodal learning (Kaufmann et al., 2023; Cheng et al., 2024). Inspired by these advances, RL-based RRG methods have shown promising results, largely due to carefully designed reward functions (Xiao et al., 2024). Prior works (Qin and Song, 2022; Zhou et al., 2024) leverage NLG or clinical efficacy (CE) metrics to align RRG models. However, such rewards provide limited evidence-based guidance. Moreover, while clinical reports require preference alignment, existing Preference-based RL (PbRL) methods (Xiao et al., 2024; Cheng et al., 2024) typically rely on report-level preference datasets and lack a self-improving mechanism to correct unreliable descriptions. To address these gaps, we propose an Evidence-aware Self-Correcting Reinforcement Learning (ESC-RL) framework, which tackles limited evidence guidance and disease-specific self-correction in report generation.

To provide effective clinical evidence-based guidance under weak supervision, we introduce a Group-wise Evidence-aware Alignment Reward (GEAR) module. GEAR enhances fine-grained image-report alignment via a group-wise alignment reward. It first compares disease-status vectors from ground-truth and generated reports, partitioning predictions into true positives (TPs), false negatives (FNs), and false positives (FPs). Using Disease-grounded Response Maps (DRMs), GEAR imposes group-wise evidence-aware constraints: (1) for TPs, it enforces precise grounding by maximizing IoUs between predicted and ground-truth DRMs; (2) for FNPs, it aims to recover missed evidence by minimizing differences between the predicted and corresponding ground-truth DRMs; and (3) for FPs, it penalizes unsupported claims by discouraging highly activated DRMs with irrele-

084 vant regions. These designs yield disease-specific,  
085 evidence-aware RL rewards that provide clinically  
086 grounded feedback for policy optimization.

087 To further align generated reports with clinical  
088 preferences, we develop a Self-correcting Prefer-  
089 ence Learning (SPL) strategy. SPL constructs a  
090 disease-specific preference dataset from multiple  
091 candidate report-level observations and uses it to  
092 train a lightweight predictor with a disease-specific  
093 description selection mechanism. Specifically, the  
094 predictor scores each disease-specific description,  
095 after which the selection mechanism identifies  
096 and filters unreliable descriptions. The retained  
097 trustworthy data then guides the re-integration of  
098 disease-specific observations to produce a more  
099 accurate, refined report. Our contributions can be  
100 summarized as follows:

- 101 • We propose a novel ESC-RL framework to  
102 integrate a Group-wise Evidence-aware Align-  
103 ment Reward (GEAR) and a Self-correcting  
104 Preference Learning (SPL) strategy to ad-  
105 dress limited evidence guidance and disease-  
106 specific self-correction in RL-based RRG.
- 107 • GEAR aligns disease-specific visual-text  
108 groundings between predicted and ground-  
109 truth reports via group-wise constraints, pro-  
110 viding disease-specific, evidence-aware feed-  
111 back for policy optimization.
- 112 • SPL identifies and selects reliable disease-  
113 level descriptions from multiple noisy gener-  
114 ated observations, enabling accurate disease-  
115 specific description refinement.
- 116 • Extensive experiments, including compar-  
117 isons with state-of-the-art RRG methods and  
118 ablation studies, consistently demonstrate the  
119 superior performance of our approach.

## 120 2 Related Works

### 121 2.1 Radiology Report Generation

122 Radiology report generation (RRG) focuses on gener-  
123 ating detailed and clinically accurate textual de-  
124 scriptions from medical images. Recent advance-  
125 ments in RRG have explored a variety of tech-  
126 niques aimed at improving the quality, relevance,  
127 and accuracy of the generated reports. These ap-  
128 proaches include knowledge graphs (Yin et al.,  
129 2025), contrastive learning (Li et al., 2024; Liu  
130 et al., 2025), retrieval-augmented methods (Zhou  
131 et al., 2025b), memory alignment (Chen et al.,

2020, 2022), reinforcement learning (Qin and Song,  
2022), human preference optimization (Xiao et al.,  
2024), and LLM-based methods (Hou et al., 2025;  
Zhang et al., 2025). Despite recent advances, ra-  
diology report generation (RRG) remains far from  
robust clinical deployment due to reliability issues,  
including omissions and hallucinations of critical  
findings, and the lack of self-improving mecha-  
nisms to align with evolving clinical preferences,  
keeping RRG an active research area.

### 142 2.2 Reinforcement Learning

143 Reinforcement learning (RL) is a learning  
144 paradigm for sequential decision-making, where  
145 an agent interacts with the environment and learns  
146 a policy to maximize cumulative rewards. RL has  
147 achieved strong empirical success across diverse  
148 domains such as gaming, robotics, finance, and  
149 healthcare (Cheng et al., 2024). Recently, RL has  
150 been explored for report generation tasks (Qin and  
151 Song, 2022; Zhou et al., 2024; Xiao et al., 2024).  
152 For example, (Qin and Song, 2022; Zhou et al.,  
153 2024) leverages NLG metrics such as BLEU, Rad-  
154 CliQ to guide cross-modal alignment between vi-  
155 sual and textual features, using these metrics as  
156 rewards for the RL process. (Xiao et al., 2024)  
157 introduces a multi-dimensional reward framework  
158 to align the generated reports with multiple hu-  
159 man preferences. Despite this progress, these  
160 methods largely depend on report-level reward  
161 signals or manually designed multi-objective re-  
162 wards, which provide limited evidence-level guid-  
163 ance and may be constrained by training-set cov-  
164 erage (Xiong et al., 2024). Alternatively, some  
165 Preference-based RL (PbRL) approaches (Chen  
166 et al., 2024; Xiao et al., 2025) construct report-level  
167 preference datasets using strong foundation mod-  
168 els and obtain preference labels via LLM-based  
169 scoring or metric-based evaluation, eliminating the  
170 requirement for manually designed reward func-  
171 tions. However, these methods align only at the  
172 report level, lacking fine-grained preference align-  
173 ment and an explicit self-improvement mechanism.

## 174 3 Methods

### 175 3.1 Preliminaries

176 Reinforcement learning (RL) based RRG aims to  
177 directly optimize report generation quality by treat-  
178 ing the report generator as an agent that interacts  
179 with an environment defined by visual evidence  
180 and previously generated text. Specifically, the

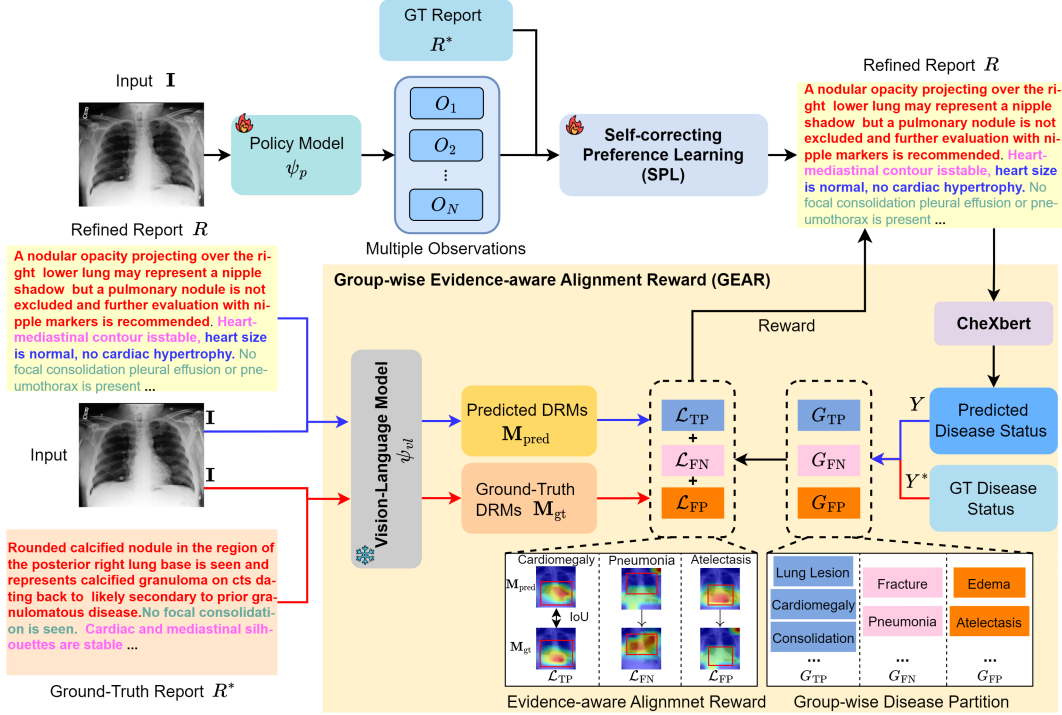


Figure 1: Overview of the proposed Evidence-aware Self-Correcting Reinforcement Learning (ESC-RL) framework.

model parameters  $\theta$  defines a policy  $\psi_p$  that determines the next action (i.e., the prediction of the next word). Given a radiology image  $\mathbf{I}$ , the probability of generating a report  $R = (y_1, \dots, y_L)$  of length  $L$  is formulated as,

$$\psi_p(R|\mathbf{I}) = \prod_{l=1}^L \psi_p(y_l|y_1, \dots, y_{l-1}, \mathbf{I}), \quad (1)$$

where  $\mathbb{V}$  denotes the vocabulary,  $y_l \in \mathbb{V}$  is a token.

Upon generating the end-of-sequence (EOS) token, the environment returns a scalar reward  $r(R)$  to evaluate the overall quality of the generated report. RL training optimizes  $\theta$  by maximizing the expected reward under the policy distribution, equivalently minimizing the negative expected reward,

$$\mathcal{L}_{\text{RL}}(\theta) = -\mathbb{E}_{R \sim \psi_p}[r(R)]. \quad (2)$$

Nevertheless, recent RL-based RRG methods (Qin and Song, 2022; Zhou et al., 2024; Chen et al., 2024; Xiao et al., 2025) still face three essential challenges: (1) the lack of fine-grained, evidence-based rewards for clinically faithful report generation; (2) the reliance on report-level preference construction for sample selection; and (3) the absence of an explicit self-correcting mechanism to support self-improvement. The proposed ESC-RL framework is explicitly designed to overcome these limitations. Details are presented in the following.

### 3.2 Framework Overview

Figure 1 illustrates the overall workflow of our ESC-RL framework. Given a chest X-ray image  $\mathbf{I} \in \mathbb{R}^{H \times W \times 3}$ , our goal is to generate a clinically accurate radiology report  $R = \{y_1, y_2, \dots, y_L\}$ , where  $(H, W)$  denotes the spatial resolution of the input image. Denote the ground-truth disease-status labels as  $Y^* \in \{0, 1, 2, 3\}^K$ , where  $K$  denotes the number of disease categories and  $\{0, 1, 2, 3\}$  correspond to blank, positive, negative, and uncertain status, respectively. The image  $\mathbf{I}$  is first fed into the policy model  $\psi_p$  to sample  $N$  candidate observations  $\{O_n\}_{n=1}^N$ . Then  $\{O_n\}_{n=1}^N$  together with the ground-truth report  $R^*$  are processed by the Self-correcting Preference Learning (SPL) module to obtain a refined report  $R$ .

To provide clinically-grounded evidence guidance, we incorporate a Group-wise Evidence-aware Alignment Reward (GEAR). GEAR compares the disease-status vectors  $Y$  and  $Y^*$  extracted from both the predicted and ground-truth reports using CheXbert, grouping predictions into true-positives (TPs), false-negatives (FNs), and false-positives (FPs). Disease-grounded Response Maps (DRMs) from the predicted and ground-truth reports are then utilized to design group-wise rewards for TPs, FN and FP, respectively, aiming to enforce consistent DRMs for TP group, promote missed DRMs

recovery for FN group, and suppress hallucinated evidence for FP group. The SPL strategy automatically scores and selects reliable disease-specific descriptions from multiple noisy observations to generate the final refined report.

### 3.3 Group-wise Evidence-aware Alignment Reward

Fine-grained evidence is crucial for clinical diagnosis, as radiologists must localize subtle abnormalities and justify report statements with corresponding image regions. Without explicit disease-evidence level annotations, existing RL-based approaches (Qin and Song, 2022; Zhou et al., 2024) often rely on coarse report-level rewards, leading to missed findings and hallucination. To mitigate this issue, we propose a novel GEAR module, as shown in Figure 1. GEAR compares Disease-grounded Response Maps (DRMs) derived from generated and ground-truth reports, and applies group-wise alignment reward to enforce region-level consistency for true-positive diseases, promote recovery for false-negative diseases, and suppress unsupported activations for false-positive diseases.

**Group-wise Disease Partition.** Given the refined report  $R$ , we use CheXbert to extract the predicted disease-status vector  $Y \in \{0, 1, 2, 3\}^K$ . Then we compare  $Y$  and the ground-truth disease-status labels  $Y^*$  to form three meaningful groups: true positives (TP), false negatives (FN), and false positives (FP). It is worth noting that negative and uncertain status are excluded during group partition for simplicity. Specifically, TP group  $G_{\text{TP}}$  contains diseases that are correctly predicted as present in both  $Y$  and  $Y^*$ :

$$G_{\text{TP}} = \{k, |Y_k^* = 1, Y_k = 1\}. \quad (3)$$

FN group  $G_{\text{FN}}$  contains diseases which are present in  $Y^*$  but missed in  $Y$ ,

$$G_{\text{FN}} = \{k, |Y_k^* = 1, Y_k = 0\}. \quad (4)$$

FP group  $G_{\text{FP}}$  contains diseases that are predicted as present in  $Y$  but absent in  $Y^*$ ,

$$G_{\text{FP}} = \{k, |Y_k^* = 0, Y_k = 1\}. \quad (5)$$

This decomposition allows GEAR to explicitly reinforce correctly recognized findings (TP), recover missed findings (FN) and suppress hallucinated findings (FP).

**Disease-grounded Response Maps (DRMs) Generation.** Given a CXR image  $\mathbf{I}$ , we use a frozen vision–language grounding model  $\psi_{vl}$  pre-trained on large-scale image–report pairs (e.g., MAVL (Phan et al., 2024)) to extract disease-grounded response maps (DRMs). Specifically, we obtain predicted DRMs  $\mathbf{M}^{\text{pred}}$  conditioned on  $\mathbf{I}$  and the generated refined report  $R$ , and ground-truth DRMs  $\mathbf{M}^{\text{gt}}$  conditioned on  $\mathbf{I}$  and the ground-truth report  $R^*$ :

$$\begin{aligned} \mathbf{M}^{\text{pred}} &= \psi_{vl}(\mathbf{I}, R) \in \mathbb{R}^{H \times W \times K}, \\ \mathbf{M}^{\text{gt}} &= \psi_{vl}(\mathbf{I}, R^*) \in \mathbb{R}^{H \times W \times K}, \end{aligned} \quad (6)$$

where  $K$  is the number of diseases, and  $(H, W)$  is the spatial resolution of the response map.

**Evidence-aware Alignment Reward.** For group  $G_{\text{TP}}$ , we enforce spatial consistency between  $\mathbf{M}^{\text{pred}}$  and  $\mathbf{M}^{\text{gt}}$  using an IoU-based loss, which promotes consistent spatial coverage between predicted and ground-truth evidence maps,

$$\begin{aligned} \mathcal{L}_{\text{TP}} = & 1 - \frac{1}{|G_{\text{TP}}|} \sum_{k \in G_{\text{TP}}} \\ & \frac{2 \sum_{h,w} \mathbf{M}_{h,w,k}^{\text{pred}} \mathbf{M}_{h,w,k}^{\text{gt}} + \epsilon}{\sum_{h,w} (\mathbf{M}_{h,w,k}^{\text{pred}})^2 + \sum_{h,w} (\mathbf{M}_{h,w,k}^{\text{gt}})^2 + \epsilon}, \end{aligned} \quad (7)$$

where  $\epsilon$  is a small constant for numerical stability.

For group  $G_{\text{FN}}$ , we encourage the predicted DRMs to match the ground-truth DRMs via an MSE objective, thus penalizing omissions and promoting evidence recovery,

$$\mathcal{L}_{\text{FN}} = -\frac{1}{|G_{\text{FN}}|} \sum_{k \in G_{\text{FN}}} \frac{1}{HW} \sum_{h,w} (\mathbf{M}_{h,w,k}^{\text{pred}} - \mathbf{M}_{h,w,k}^{\text{gt}})^2. \quad (8)$$

For group  $G_{\text{FP}}$ , we suppress unsupported activations by penalizing the response energy of  $\mathbf{M}^{\text{pred}}$ , which discourages the model from producing strong visual evidence for hallucinated findings,

$$\mathcal{L}_{\text{FP}} = \frac{1}{|G_{\text{FP}}|} \sum_{k \in G_{\text{FP}}} \frac{1}{HW} \sum_{h,w} (\mathbf{M}_{h,w,k}^{\text{pred}})^2. \quad (9)$$

The overall group-wise alignment reward  $\mathcal{L}_{\text{R}}$  combines rewards from the three groups as,

$$\mathcal{L}_{\text{R}} = \mathcal{L}_{\text{TP}} + \mathcal{L}_{\text{FN}} + \mathcal{L}_{\text{FP}}. \quad (10)$$

### 3.4 Self-correcting Preference Learning

The Self-correcting Preference Learning (SPL) strategy is designed to enable self-improvement

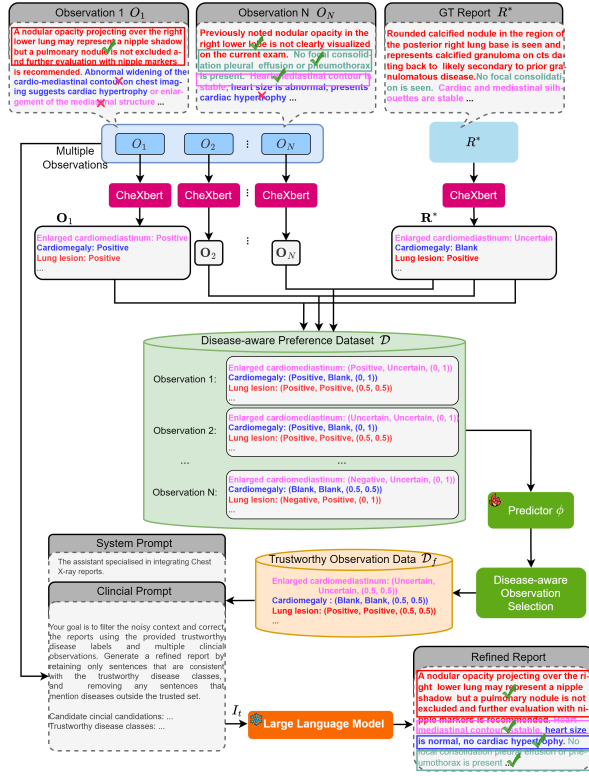


Figure 2: Illustration of the Self-correcting Preference Learning (SPL) module.

to better align with clinical preference. SPL constructs a disease-aware preference dataset from multiple noisy observations without human supervision, and automatically learns a predictor and selector to identify and filter unreliable disease descriptions. The overall workflow of SPL is illustrated in Figure 2.

### Disease-aware Preference Dataset Construction.

Given  $N$  candidate observations  $\{O_n\}_{n=1}^N$  generated by the policy model  $\psi_p$ , we first apply CheXbert to extract a disease-status vector for each observation. We also extract the ground-truth disease-status vector from the target report. To facilitate preference learning at the disease level, we convert the disease-status vector into clinically meaningful natural-language disease descriptions. Specifically, for the  $n$ -th observation, we obtain  $O_n = \{O_n^k\}_{k=1}^K$ , and for the ground-truth report we obtain  $R^* = \{R^{*k}\}_{k=1}^K$ , where  $O_n^k$  and  $R^{*k}$  denote the textual descriptions associated with the  $k$ -th disease. We then construct disease-specific pairwise preference dataset in two steps:

(1) Dataset Construction. For the  $k$ -th disease category in observation  $O_n$ , we form a pair  $(O_n^k, R^{*k})$ , and finally result in a set of disease-wise pairs  $\{(O_n^k, R^{*k})\}_{n=1, k=1}^{N, K}$ ;

(2) Quality Scoring. For each pair  $(O_n^k, R^{*k})$ , we assign a two-dimensional preference label  $\tilde{\delta}_n^k \in \{(1, 0), (0, 1), (0.5, 0.5)\}$  according to the relationship between  $O_n^k$  and  $R^{*k}$ . Specifically,  $(1, 0)$  indicates that  $O_n^k$  is consistent with  $R^{*k}$  for disease  $k$ ,  $(0, 1)$  indicates that  $R^{*k}$  is inconsistent with  $O_n^k$  for disease  $k$ , and  $(0.5, 0.5)$  denotes an indistinguishable case where  $O_n^k$  cannot be reliably judged as correct or incorrect with respect to  $R^{*k}$ . In our method, the preference is determined with  $R^{*k}$  as the reference according to LLMs. Each disease description is then stored as a triplet  $(O_n^k, R^{*k}, \tilde{\delta}_n^k)$  in the disease-aware preference dataset  $\mathcal{D}$ , which is subsequently used to train the predictor model  $\phi$ .

**Preference Learning.** The continual policy updates in RL induce a non-stationary sampling distribution, leading to noisy and unstable weak preference labels. Inspired by (Cheng et al., 2024), we use a dual-threshold sample selector to filter and preserve reliable samples. Concretely, for each disease-aware preference pair  $(O_n^k, R^{*k})$ , we use the preference predictor  $\phi$  to produce a categorical distribution  $\phi(O_n^k, R^{*k})$ . We measure the reliability of the pair by the divergence between the target distribution and the predicted distribution:  $D_{\text{KL}}(\tilde{\delta}_n^k | \phi(O_n^k, R^{*k}))$ . Intuitively, pairs with large divergence are likely to be mislabeled or inconsistent and are therefore removed. Following (Cheng et al., 2024), we select a trustworthy subset  $\mathcal{D}_f$  from the original preference dataset  $\mathcal{D}$  via the lower bound  $\tau_{\text{lower}}$  and upper bound  $\tau_{\text{upper}}$  as follows,

$$\mathcal{D}_f = \left\{ (O_n^k, R^{*k}, \tilde{\delta}_n^k) \mid \tau_{\text{lower}} < D_{\text{KL}}(\tilde{\delta}_n^k \parallel \phi(O_n^k, R^{*k})) < \tau_{\text{upper}} \right\}, \quad (11)$$

where  $\phi(O_n^k, R^{*k})$  denote the predictor’s output distribution and  $\tilde{\delta}_n^k$  is the corresponding target distribution.  $\tau_{\text{upper}}$  is a time-varying threshold.

The predictor is optimized with a standard cross-entropy objective,

$$\mathcal{L}_P = \mathbb{E}_{(O_n^k, R^{*k}, \tilde{\delta}_n^k) \sim \mathcal{D}} [\text{CE}(\phi(O_n^k, R^{*k}), \tilde{\delta}_n^k)]. \quad (12)$$

The filtered set  $\mathcal{D}_f$  is subsequently used to guide observation selection and report re-integration.

**LLM-guided Self-correcting.** Considering the excellent text generation and structured reasoning capabilities of large language models (LLMs), we employ LLM as a report re-integration component to consolidate multiple candidate observations into a refined report. Given the candidate observations

$\{O_n\}_{n=1}^N$  and the trustworthy observation data  $\mathcal{D}_f$ , we construct a structured prompt  $I_t$  that consists of: (i) a system prompt (ii) an instruction that enforces consistency with  $\mathcal{D}_f$  and the candidate observations  $\{O_n\}_{n=1}^N$ . The prompt  $I_t$  is then fed into the LLM, which removes sentences that violate  $\mathcal{D}_f$ , retains clinically supported descriptions, and integrates the remaining information into a coherent refined report  $R$ .

### 3.5 Training and Inference

The overall objective is formulated as,

$$\mathcal{L} = \mathcal{L}_{\text{task}} + \gamma \mathcal{L}_R + \mathcal{L}_P, \quad (13)$$

where  $\gamma$  is a hyperparameter and set to 0.5 by default, and  $\mathcal{L}_{\text{task}}$  is the loss of policy model.

During inference, given an input image  $\mathbf{I}$ , we first sample multiple candidate reports via the policy model  $\psi_p$ . The SPL module then filters unreliable disease-specific predictions. Finally, using the retained trustworthy signals and candidate observations, the LLM prompted with a tailored instruction, produces the final refined report.

## 4 Experiments

In this section, we demonstrate the effectiveness of our framework through comprehensive comparisons. Owing to space constraints, we present further visualization results and ablation experiments in the [Appendix](#).

### 4.1 Datasets and Experiment Setting

**Datasets.** We evaluate on two public datasets: MIMIC-CXR and IU-Xray. MIMIC-CXR (Johnson et al., 2019) contains 337,110 chest X-ray images and 227,835 corresponding reports. We follow the standard train/val/test splits from (Chen et al., 2020, 2022). IU-Xray (Dina et al., 2015) contains 7,470 chest X-ray images paired with 3,955 reports, and each report corresponds to either a single frontal view or a frontal-lateral view pair. We use the same data partition protocol as (Chen et al., 2020, 2022) for a fair comparison. Due to the scarcity of positives for certain diseases in the IU-Xray test set, we follow (Jin et al., 2024; Zhou et al., 2025b) to evaluate the model trained on MIMIC-CXR directly on the full IU-Xray dataset.

**Evaluation Metrics.** We report both lexical and radiology-specific metrics. For lexical evaluation, we report BLEU1, BLEU4 (Papineni et al., 2002), ROUGE-L (Lin, 2004), and BERTScore (Zhang

et al., 2020) to measure textual similarity and overall language quality. For radiology-specific evaluation, we adopt RadCliQ (Yu et al., 2022), RadGraphF1 (Jain et al., 2021), CheXbertF1 (Smit et al., 2020), and GREEN (Ostmeier et al., 2024). For all metrics except RadCliQ, higher scores indicate better performance. We also assess disease-level clinical efficacy (CE) via precision, recall, and F1, using CheXbert to map reports to 14 disease labels.

**Implementation Details.** We employ pre-trained REVTAf (Zhou et al., 2025b) as the policy model and frozen MAVL (Phan et al., 2024) for extracting Disease-grounded Response Maps from 224-resized images. We use GPT-5 as the integration LLM and preference determination. The number of candidate observations  $N$  is set to 4. Filtering thresholds are set to  $\tau_{\text{lower}} = 3 \ln(10)$  with a decay rate  $\frac{1}{30}$ , and a time-varying adaptive  $\tau_{\text{upper}}$  following (Cheng et al., 2024). We optimize with AdamW (weight decay 0.05), an initial learning rate of  $5e-5$ , and a cosine learning rate schedule. We train for 6 epochs with a batch size of 18. All experiments are conducted on an NVIDIA A800 GPU (80GB) for about 20 hours using Python 3.10, PyTorch 2.4.0, and Ubuntu 22.04.

### 4.2 Comparison with State-of-the-Arts

**Quantitative Results.** We compare ESC-RL with representative RRG methods, including the **traditional** methods R2Gen (Chen et al., 2020), R2GenCMN (Chen et al., 2022), RGRG (Tanida et al., 2023), MiniGPT-Med (Alkhaldi et al., 2024), PromptMRG (Jin et al., 2024), MedVersa (Zhou et al., 2025a), REVTAf (Zhou et al., 2025b), as well as **RL-based** approaches R2GenRL (Qin and Song, 2022), CheXagent (Chen et al., 2024), MPO (Xiao et al., 2024), OISA (Xiao et al., 2025). Detailed results on MIMIC-CXR and IU-Xray are reported in Tables 1, 2, and 3. On MIMIC-CXR dataset, as shown in Table 1, our method achieves SOTA performance on both lexical and radiology-specific metrics, consistently exceeding the second-best method. Concretely, our method obtains the absolute gains of 2.2%, 1.7%, 1.6%, 1.1%, 6%, 1.5%, 0.6%, and 1.3% over runner-up across the evaluated metrics. On the IU-Xray dataset, we follow (Jin et al., 2024; Zhou et al., 2025b) to directly evaluate the full dataset using the model pretrained on MIMIC-CXR dataset. As illustrated in Table 2, our method delivers the best overall performance

Model	Year	Lexical Metrics				Radiology Metrics			
		BLEU-1 ↑	BLEU-4 ↑	ROUGE ↑	BERTScore ↑	RadCliQ ↓	RadGraphF1 ↑	CheXbertF1 ↑	GREEN ↑
R2Gen	ACL 2020	0.353	0.103	0.277	0.886	2.89	0.195	0.276	0.306
R2GenCMN	ACL 2021	0.353	0.106	0.278	0.867	2.87	0.199	0.278	0.308
RGRG	CVPR 2023	0.373	0.126	0.264	0.873	2.85	0.221	0.284	0.313
MiniGPT-Med	-	0.191	0.012	-	0.636	2.95	0.164	0.172	0.211
PromptMRG	AAAI 2024	0.398	0.112	0.268	0.857	2.77	0.227	0.476	0.289
MedVersa	-	0.280	0.090	-	0.711	<b>2.45</b>	<b>0.289</b>	0.471	<b>0.381</b>
REVTAF	ICCV 2025	<b>0.465</b>	<b>0.182</b>	<b>0.336</b>	<b>0.887</b>	2.48	0.279	0.514	0.344
R2GenRL	ACL 2022	0.381	0.109	0.287	0.871	2.83	0.214	0.292	0.315
CheXagent	AAAI 2024	0.172	0.021	-	0.669	2.88	0.19	0.265	0.268
MPO	AAAI 2025	0.416	0.139	0.309	0.878	2.63	0.257	0.353	0.324
OISA	ACL 2025	0.428	0.129	-	0.885	2.54	0.273	<b>0.516</b>	0.341
ESC-RL (Ours)	-	<b>0.487</b>	<b>0.199</b>	<b>0.352</b>	<b>0.898</b>	<b>2.39</b>	<b>0.304</b>	<b>0.522</b>	<b>0.394</b>

Table 1: Comparison with existing RRG methods on the MIMIC-CXR dataset. The best and second-best results are highlighted in **bold** and **blue**, respectively. ‘-’ indicates not reported.

Model	Year	Lexical Metrics				Radiology Metrics			
		BLEU-1 ↑	BLEU-4 ↑	ROUGE ↑	BERTScore ↑	RadCliQ ↓	RadGraphF1 ↑	CheXbertF1 ↑	GREEN ↑
R2Gen	ACL 2020	0.289	0.052	0.243	0.861	2.79	0.187	0.154	0.482
R2GenCMN	ACL 2021	0.289	0.055	0.246	0.864	2.78	0.190	0.157	0.483
RGRG	CVPR 2023	0.266	0.063	0.180	0.867	2.71	0.189	0.155	0.481
PromptMRG	AAAI 2024	0.401	0.098	0.281	0.871	2.60	0.274	0.211	0.457
MedVersa	-	0.247	0.047	-	0.884	2.71	0.209	0.217	0.516
REVTAF	ICCV2025	<b>0.420</b>	<b>0.107</b>	<b>0.309</b>	<b>0.886</b>	<b>2.54</b>	<b>0.287</b>	<b>0.223</b>	<b>0.522</b>
R2GenRL	ACL 2021	0.290	0.054	0.248	0.865	2.78	0.192	0.157	0.487
CheXagent	AAAI 2024	0.191	0.036	-	0.876	2.81	0.184	0.097	0.407
ESC-RL (Ours)	-	<b>0.439</b>	<b>0.118</b>	<b>0.323</b>	<b>0.890</b>	<b>2.48</b>	<b>0.307</b>	<b>0.231</b>	<b>0.537</b>

Table 2: Comparison with existing RRG methods on the IU-Xray dataset. The best and second-best results are highlighted in **bold** and **blue**, respectively. ‘-’ indicates not reported.

across all lexical and radiology-specific metrics, outperforming the second-best method REVTAF by 1.9%, 1.1%, 1.4%, 0.4%, 6%, 2.0%, 0.8%, and 1.5%, respectively. For CE metrics, as shown in Table 3, our ESC-RL consistently surpasses the second-best method REVTAF. Specifically, on the MIMIC-CXR dataset, it achieves gains of by 0.4%, 1.2%, and 1.6% in Precision, Recall, and F1, respectively. On the IU-Xray dataset, the corresponding improvements are 1.3%, 2.9%, and 2.2%. Overall, ESC-RL consistently outperforms the second-best method across all reported metrics on both datasets.

Model	MIMIC-CXR			IU-Xray		
	Precision	Recall	F1	Precision	Recall	F1
R2Gen	0.333	0.273	0.276	0.151	0.145	0.145
R2GenCMN	0.334	0.275	0.278	0.154	0.147	0.147
RGRG	0.461	0.475	0.447	0.183	0.187	0.180
PromptMRG	0.501	0.509	0.476	0.213	0.229	0.211
REVTAF	<b>0.628</b>	<b>0.613</b>	<b>0.592</b>	<b>0.286</b>	<b>0.282</b>	<b>0.273</b>
R2GenRL	0.334	0.275	0.278	0.153	0.150	0.151
MPO	0.436	0.376	0.353	-	-	-
ESC-RL (Ours)	<b>0.632</b>	<b>0.625</b>	<b>0.608</b>	<b>0.299</b>	<b>0.311</b>	<b>0.295</b>

Table 3: Clinical Efficacy (CE) comparison of 14 diseases on the MIMIC-CXR and IU-Xray datasets. Best values are highlighted in **bold** and second-best in **blue**.

**Qualitative Results.** Figure 3 presents two qualitative examples highlighting the superiority of ESC-RL over SOTA methods. As observed, ESC-RL recovers key report content, accurately identifying

support devices and major findings such as cardio-mediastinal contours, cardiomegaly, and atelectasis. Moreover, ESC-RL captures fine-grained, location-specific abnormalities, e.g., left retrocardiac atelectasis and confluent opacity in the right infrahilar region. For ambiguous signs such as a ‘hazy right lung opacity’, ESC-RL offers clinically plausible differentials: ‘aspiration, pleural effusion, or hemorrhage’, consistent with the ground-truth. In contrast, R2GenRL, PromptMRG, and REVTAF often yield factual errors, incomplete descriptions, and insufficient interpretations. Overall, ESC-RL better suppresses hallucinated content and generates more accurate clinical findings, further validating the effectiveness of the proposed framework.

### 4.3 Ablation Study

We validate the effectiveness of each component in our model on the MIMIC-CXR test set, as shown in Table 4. As observed, introducing the RL framework, GEAR module, or SPL consistently improves performance over the baseline. RL alone improves GREEN by 0.5%, indicating that report-level rewards effectively enhance cross-modal alignment. GEAR alone boosts GREEN by 1.4%, supporting the benefit of evidence-aware reward shaping for clinically aligned grounding. SPL alone yields a 1.2% gain in GREEN, demon-



Image	R2GenRL Generated Report	PromptMRG Generated Report	REVTAF Generated Report	ESC-RL (Ours) Generated Report	Ground-Truth Report
	Intubating support and monitoring devices remain unchanged in position. The cardiomeastinal silhouette is stable. There is mild pulmonary vascular congestion with minimal interstitial edema. Patchy and linear bibasilar opacities are present, likely representing atelectasis, although aspiration or infection cannot be excluded. A small left pleural effusion is noted. No pneumothorax is identified.	Support and monitoring devices are unchanged in position. Cardiomeastinal contours are stable. Right retrocardiac atelectasis has improved, while a new area of increased opacity is noted in the left infrahilar region. These findings may reflect atelectasis or developing infection. No pleural effusion is seen.	Intubating support and monitoring devices are unchanged in position and cardiomeastinal contours are stable in appearance. Pulmonary vascular congestion is accompanied by minimal interstitial edema. Patchy and linear bibasilar opacities probably represent atelectasis but coexisting aspiration or infectious pneumonia is also possible in the appropriate clinical setting. Small left pleural effusion is also noted.	Intubating support and monitoring devices are unchanged in position. Cardiomegaly and mediastinal contours are stable. Left retrocardiac atelectasis has improved. A new confluent opacity is present in the right infrahilar region, which may represent atelectasis, aspiration, or developing infection. No pleural effusion or pneumothorax is identified.	Intubating support and monitoring devices are unchanged in position, and cardiomeastinal contours are stable allowing for positional differences. Left retrocardiac atelectasis has improved, but an area of confluent increased opacity in the right infrahilar region is new. The latter may reflect atelectasis, aspiration, or developing infection.
	Lung volumes are mildly reduced. The heart is moderately enlarged and stable. The thoracic aorta is tortuous with atherosclerotic calcifications. There is perihilar haziness with vascular indistinctness, compatible with moderate pulmonary edema. Small bilateral pleural effusions are present. Bilateral airspace opacities likely represent atelectasis. A hazy opacity is noted in the right lung, which may reflect aspiration.	An endotracheal tube is present with the tip above the carina. The cardiac silhouette is moderately enlarged. Prominence of the pulmonary vasculature with cephalization suggests mild pulmonary edema. A focal right lung opacity is seen, favored to represent pulmonary hemorrhage. No pneumothorax or displaced rib fractures are identified.	Tracheostomy tube is in standard position. Lung volumes are low. Heart size is moderately enlarged. The aorta is tortuous and demonstrates atherosclerotic calcifications. Perihilar haziness with vascular indistinctness is compatible with moderate pulmonary edema. Small bilateral pleural effusions are likely present. Bilateral airspace opacities likely reflect areas of atelectasis. No pneumothorax is identified. There are no acute osseous abnormalities.	A tracheostomy tube is in standard position. Moderate cardiomegaly is stable. There is slight prominence of the pulmonary vasculature with cephalization and enlarged pulmonary arteries consistent with mild pulmonary edema. Hazy opacity is present in the right lung, which may represent aspiration, pleural effusion or hemorrhage. A retrocardiac opacity at the left lung base is unchanged. Moderate cardiomegaly is stable. Slight prominence of the pulmonary vasculature with cephalization and enlarged pulmonary arteries are consistent with mild pulmonary edema. Tracheostomy tube is in place. There are no displaced rib fractures.	A hazy opacity is present in the right lung which may represent aspiration, pleural effusion or hemorrhage. Retrocardiac opacity at the left base is unchanged. Moderate cardiomegaly is stable. Slight prominence of the pulmonary vasculature with cephalization and enlarged pulmonary arteries are consistent with mild pulmonary edema. Tracheostomy tube is in place. There are no displaced rib fractures.

Figure 3: Qualitative comparison of reports generated by R2GenRL, PromptMRG, REVTAF, and our method. Sentences are color-coded to indicate their corresponding descriptions. Incorrect statements are marked with ×, and unmarked sentences denote descriptions not mentioned in the ground-truth report.

Setting	RL	GEAR	SPL	Lexical Metrics				Radiology Metrics			
				BLEU-1 ↑	BLEU-4 ↑	ROUGE ↑	BERTScore ↑	RadCliQ ↓	RadGraphF1 ↑	CheXbertF1 ↑	GREEN ↑
Baseline				0.465	0.182	0.336	0.887	2.48	0.279	0.514	0.344
(a)	✓			0.472	0.187	0.335	0.889	2.45	0.282	0.517	0.349
(b)		✓		0.471	0.191	0.334	0.891	2.42	0.285	0.518	0.358
(c)			✓	0.475	0.190	0.339	0.892	2.40	0.288	0.517	0.356
(d)	✓	✓		0.481	0.194	0.345	0.890	2.40	0.289	0.517	0.359
(e)	✓	✓	✓	0.483	0.195	0.344	0.892	2.40	0.297	0.519	0.364
(f)	✓	✓	✓	0.485	0.197	0.347	0.895	2.39	0.299	0.520	0.387
(g)	✓	✓	✓	<b>0.487</b>	<b>0.199</b>	<b>0.352</b>	<b>0.898</b>	<b>2.39</b>	<b>0.304</b>	<b>0.522</b>	<b>0.394</b>

Table 4: Effectiveness analysis of each component on MIMIC-CXR test set.

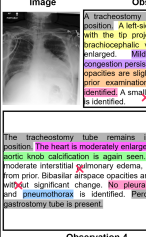
Image	Observation 1	Observation 2	Observation 3
	A tracheostomy tube is present in stable position. A left-sided PICC line is visualized with the tip projecting over the distal left brachiocephalic vein. The heart is mildly enlarged. Mild pulmonary vascular congestion persists. Bilateral linear airspace opacities are slightly improved compared to prior examination. No pleural effusion is identified. A small right apical pneumothorax is identified.	Left-sided PICC terminates in the distal left brachiocephalic vein. A small left pleural effusion is present. No pneumothorax is identified. A percutaneous gastrostomy tube is seen in the left upper quadrant. The cardiac silhouette is moderately enlarged. Kerley B-line calcification is present. Mild pulmonary vascular congestion is noted. Bilateral linear airspace opacities are slightly improved compared to prior examination. No pleural effusion is identified. No pneumothorax is identified. Percutaneous gastrostomy tube is present.	A tracheostomy tube is in place. A left-sided PICC terminates in the mid superior vena cava. The heart is mildly enlarged. The thoracic aorta is calcified. There is mild interstitial pulmonary edema. Small bilateral pleural effusions are present. Bilateral linear airspace opacities likely reflect atelectasis. There is no pneumothorax.
	The tracheostomy tube remains in stable position. The heart is moderately enlarged. Marked Kerley B-line calcification is again seen. There is moderate interstitial pulmonary edema, increased from prior. Bilateral linear airspace opacities are present without significant change. No pleural effusion and pneumothorax is identified. Percutaneous gastrostomy tube is present.	The tracheostomy tube remains in stable position. A left-sided PICC line is visualized with the tip projecting over the distal left brachiocephalic vein. The cardiac silhouette is moderately enlarged. The thoracic aorta is calcified. Mild pulmonary vascular congestion is noted. Bilateral linear airspace opacities are slightly improved compared to prior examination. No pleural effusion is identified. No pneumothorax is identified. Percutaneous gastrostomy tube is present.	Left PICC tip is seen terminating in the region of the distal left brachiocephalic vein. Tracheostomy tube is in unchanged standard position. The heart is moderately enlarged. Marked calcification of the thoracic knob is again present. Mild pulmonary vascular congestion is similar. Bilateral linear airspace opacities are mildly improved. Previously noted left pleural effusion appears to have resolved. No pneumothorax is identified. Percutaneous gastrostomy tube is seen in the left upper quadrant.
	Observation 4	Refined Report	Ground-Truth Report

Figure 4: An example of re-integrating multiple observations into a refined report. Sentences are color-coded to indicate their corresponding descriptions. Incorrect statements are highlighted with ×, and unmarked sentences denote content that is not mentioned in the ground-truth report.

strating the effectiveness of self-correcting preference learning. Moreover, based on RL, introducing either GEAR or SPL yields complementary gains beyond report-level rewards. Ultimately, integrating all proposed components, our model achieves consistent gains across all metrics, improving BLEU-1, RadGraphF1, and GREEN by 2.2%, 2.5%, and 5.0%, respectively. These results highlight indispensable role of these modules in achieving stronger evidence-based clinical alignment and accurate report generation.

Figure 4 illustrates a representative case where SPL re-integrates multiple intermediate observations into a refined report. As shown, observations

1–4 still contain several factual inaccuracies. After applying SPL, these errors are largely corrected, producing a refined report that better matches the ground-truth in both factual consistency and content coverage. This further validates the effectiveness of the proposed SPL strategy.

## 5 Conclusion

We propose a novel clinically aligned Evidence-aware Self-Correcting Reinforcement Learning (ESC-RL) framework for RRG. ESC-RL introduces a Group-wise Evidence-aware Alignment Reward (GEAR) module that compares disease-status vectors from ground-truth and generated reports, and groups findings into TPs, FNs, and FPs. Using DRMs, GAER enforces consistent grounding for TPs, encourages recovery of missed evidence for FNs, and suppresses hallucinated evidence for FPs. Additionally, ESC-RL incorporates a Self-correcting Preference Learning (SPL) strategy that constructs a disease-aware preference dataset and uses it to train a lightweight predictor with disease-specific description selection mechanism. SPL filters unreliable disease descriptions and leverages the retained trustworthy data to guide the observations re-integration. Extensive experiments on two public chest X-ray datasets demonstrate consistent gains and state-of-the-art performance.

## 6 Limitations

Our experiment mainly focus on chest X-ray datasets, since they provide large-scale paired images and high-quality reports. Therefore, the generalization of ESC-RL to other modalities (e.g., CT/MRI) or anatomical regions remains to be validated. In addition, our framework relies on pre-trained model to extract disease label and response maps which may introduces additional computational overhead. Future work will extend ESC-RL toward a more modality-agnostic and unified RL framework across diverse imaging settings.

## 7 Ethical Considerations

Our study uses real-world patient data from the MIMIC-CXR and IU-Xray datasets. These datasets are de-identified and released under controlled access for research purposes. Therefore, the risk of privacy leakage is minimal. We follow the corresponding data use agreements and use the data solely for developing and evaluating automated RRG models.

## References

Asma Alkhalidi, Raneem Alnajim, Layan Alabdullatef, Rawan Alyahya, Jun Chen, Deyao Zhu, Ahmed Alsinan, and Mohamed Elhoseiny. 2024. [Minigt-med: Large language model as a general interface for radiology diagnosis](#). *Preprint*, arXiv:2407.04106.

Zhihong Chen, Yaling Shen, Yan Song, and Xiang Wan. 2022. [Cross-modal memory networks for radiology report generation](#). *Preprint*, arXiv:2204.13258.

Zhihong Chen, Yan Song, Tsung-Hui Chang, and Xiang Wan. 2020. Generating radiology reports via memory-driven transformer. *arXiv preprint arXiv:2010.16056*.

Zhihong Chen, Maya Varma, Jean-Benoit Delbrouck, Magdalini Paschali, Louis Blankemeier, Dave Van Veen, Jeya Maria Jose Valanarasu, Alaa Youssef, Joseph Paul Cohen, Eduardo Pontes Reis, Emily B. Tsai, Andrew Johnston, Cameron Olsen, Tanishq Mathew Abraham, Sergios Gatidis, Akshay S Chaudhari, and Curtis Langlotz. 2024. [Chexagent: Towards a foundation model for chest x-ray interpretation](#). *arXiv preprint arXiv:2401.12208*.

Jie Cheng, Gang Xiong, Xingyuan Dai, Qinghai Miao, Yisheng Lv, and Fei-Yue Wang. 2024. RIME: Robust preference-based reinforcement learning with noisy preferences. In *Proceedings of the 41st International Conference on Machine Learning*, volume 235, pages 8229–8247. PMLR.

Demner Fushman Dina, Marc D Kohli, Marc B Rosenman, Sonya E Shooshan, Rodriguez Laritza, Antani Sameer, George R Thoma, and Clement J Mcdonald. 2015. Preparing a collection of radiology examinations for distribution and retrieval. *Journal of the American Medical Informatics Association Jamia*, (2):2.

Wenjun Hou, Yi Cheng, Kaishuai Xu, Heng Li, Yan Hu, Wenjie Li, and Jiang Liu. 2025. [Radar: Enhancing radiology report generation with supplementary knowledge injection](#). *Preprint*, arXiv:2505.14318.

Saahil Jain, Ashwin Agrawal, Adriel Saporta, Steven QH Truong, Du Nguyen Duong, Tan Bui, Pierre Chambon, Yuhao Zhang, Matthew P. Lungren, Andrew Y. Ng, Curtis P. Langlotz, and Pranav Rajpurkar. 2021. [Radgraph: Extracting clinical entities and relations from radiology reports](#). *Preprint*, arXiv:2106.14463.

Haibo Jin, Haoxuan Che, Yi Lin, and Hao Chen. 2024. [Promptmrg: Diagnosis-driven prompts for medical report generation](#). In *Proceedings of the AAAI Conference on Artificial Intelligence*, volume 38, pages 2607–2615.

Alistair E. W. Johnson, Tom J. Pollard, Nathaniel R. Greenbaum, Matthew P. Lungren, Chih ying Deng, Yifan Peng, Zhiyong Lu, Roger G. Mark, Seth J. Berkowitz, and Steven Horng. 2019. [Mimic-cxr-jpg, a large publicly available database of labeled chest radiographs](#). *Preprint*, arXiv:1901.07042.

Elia Kaufmann, Leonard Bauersfeld, Antonio Loquercio, Matthias Müller, Vladlen Koltun, and Davide Scaramuzza. 2023. Champion-level drone racing using deep reinforcement learning. *Nature*, 620(7976):982–987.

Mingjie Li, Haokun Lin, Liang Qiu, Xiaodan Liang, Ling Chen, Abdulmotaleb Elsaddik, and Xiaojun Chang. 2024. [Contrastive learning with counterfactual explanations for radiology report generation](#). *Preprint*, arXiv:2407.14474.

Chin-Yew Lin. 2004. [ROUGE: A package for automatic evaluation of summaries](#). In *Text Summarization Branches Out*, pages 74–81, Barcelona, Spain. Association for Computational Linguistics.

Kang Liu, Zhuoqi Ma, Xiaolu Kang, Yunan Li, Kun Xie, Zhicheng Jiao, and Qiguang Miao. 2025. [Enhanced contrastive learning with multi-view longitudinal data for chest x-ray report generation](#). In *2025 IEEE/CVF Conference on Computer Vision and Pattern Recognition (CVPR)*, page 10348–10359. IEEE.

Sophie Ostmeier, Justin Xu, Zhihong Chen, Maya Varma, Louis Blankemeier, Christian Bluethgen, Arne Edward Michalson Md, Michael Moseley, Curtis Langlotz, Akshay S Chaudhari, and Jean-Benoit Delbrouck. 2024. [Green: Generative radiology report evaluation and error notation](#). In *Findings of the Association for Computational Linguistics: EMNLP 2024*, page 374–390. Association for Computational Linguistics.

675	Kishore Papineni, Salim Roukos, Todd Ward, and Weijing Zhu. 2002. <a href="#">Bleu: a method for automatic evaluation of machine translation</a> . In <i>Proceedings of the 40th Annual Meeting of the Association for Computational Linguistics</i> , pages 311–318, Philadelphia, Pennsylvania, USA. Association for Computational Linguistics.	730
676		731
677		732
678		733
679		734
680		735
681		736
682	Vu Minh Hieu Phan, Yutong Xie, Yuankai Qi, Lingqiao Liu, Liyang Liu, Bowen Zhang, Zhibin Liao, Qi Wu, Minh-Son To, and Johan W Verjans. 2024. Decomposing disease descriptions for enhanced pathology detection: A multi-aspect vision-language pre-training framework. In <i>Proceedings of the IEEE/CVF Conference on Computer Vision and Pattern Recognition</i> , pages 11492–11501.	737
683		738
684		739
685		740
686		741
687		742
688		743
689		744
690	Han Qin and Yan Song. 2022. <a href="#">Reinforced cross-modal alignment for radiology report generation</a> . In <i>Findings of the Association for Computational Linguistics: ACL 2022</i> , pages 448–458, Dublin, Ireland. Association for Computational Linguistics.	745
691		746
692		747
693		748
694		749
695	Akshay Smit, Saahil Jain, Pranav Rajpurkar, Anuj Pareek, Andrew Y. Ng, and Matthew P. Lungren. 2020. <a href="#">Chexbert: Combining automatic labelers and expert annotations for accurate radiology report labeling using bert</a> . <i>Preprint</i> , arXiv:2004.09167.	750
696		751
697		752
698		753
699		754
700	Tim Tanida, Philip Müller, Georgios Kaissis, and Daniel Rueckert. 2023. <a href="#">Interactive and explainable region-guided radiology report generation</a> . In <i>2023 IEEE/CVF Conference on Computer Vision and Pattern Recognition (CVPR)</i> , page 7433–7442. IEEE.	755
701		756
702		757
703		758
704		759
705	Chaoyi Wu, Xiaoman Zhang, Ya Zhang, Yanfeng Wang, and Weidi Xie. 2023. Medklip: Medical knowledge enhanced language-image pre-training. <i>Proceedings of the IEEE/CVF International Conference on Computer Vision</i> .	760
706		761
707		762
708		763
709		764
710	Ting Xiao, Lei Shi, Peng Liu, Zhe Wang, and Chenjia Bai. 2024. <a href="#">Radiology report generation via multi-objective preference optimization</a> . <i>Preprint</i> , arXiv:2412.08901.	765
711		766
712		767
713		768
714	Ting Xiao, Lei Shi, Yang Zhang, HaoFeng Yang, Zhe Wang, and Chenjia Bai. 2025. <a href="#">Online iterative self-alignment for radiology report generation</a> . <i>Preprint</i> , arXiv:2505.11983.	769
715		770
716		771
717		772
718	Wei Xiong, Hanze Dong, Chenlu Ye, Ziqi Wang, Han Zhong, Heng Ji, Nan Jiang, and Tong Zhang. 2024. <a href="#">Iterative preference learning from human feedback: Bridging theory and practice for rlhf under kl-constraint</a> . <i>Preprint</i> , arXiv:2312.11456.	773
719		774
720		775
721		776
722		777
723	Heng Yin, Shanlin Zhou, Pandong Wang, Zirui Wu, and Yongtao Hao. 2025. <a href="#">KIA: Knowledge-guided implicit vision-language alignment for chest X-ray report generation</a> . In <i>Proceedings of the 31st International Conference on Computational Linguistics</i> , pages 4096–4108, Abu Dhabi, UAE. Association for Computational Linguistics.	778
724		779
725		780
726		781
727		
728		
729		
	Feiyang Yu, Mark Endo, Rayan Krishnan, Ian Pan, Andy Tsai, Eduardo Pontes Reis, Eduardo Kaiser Ururahy Nunes Fonseca, Henrique Min Ho Lee, Zahra Shakeri Hossein Abad, Andrew Y. Ng, Curtis P. Langlotz, Vasantha Kumar Venugopal, and Pranav Rajpurkar. 2022. <a href="#">Evaluating progress in automatic chest x-ray radiology report generation</a> . <i>medRxiv</i> .	
	Tianyi Zhang, Varsha Kishore, Felix Wu, Kilian Q. Weinberger, and Yoav Artzi. 2020. <a href="#">Bertscore: Evaluating text generation with bert</a> . <i>Preprint</i> , arXiv:1904.09675.	
	Xi Zhang, Zaiqiao Meng, Jake Lever, and Edmond S. L. Ho. 2025. <a href="#">Libra: Leveraging temporal images for biomedical radiology analysis</a> . <i>Preprint</i> , arXiv:2411.19378.	
	Hong-Yu Zhou, Julián Nicolás Acosta, Subathra Adithan, Suvrankar Datta, Eric J. Topol, and Pranav Rajpurkar. 2025a. <a href="#">Medversa: A generalist foundation model for medical image interpretation</a> . <i>Preprint</i> , arXiv:2405.07988.	
	Qin Zhou, Guoyan Liang, Xindi Li, Jingyuan Chen, Wang Zhe, Chang Yao, and Sai Wu. 2025b. <a href="#">Learnable retrieval enhanced visual-text alignment and fusion for radiology report generation</a> . <i>Preprint</i> , arXiv:2507.07568.	
	Zijian Zhou, Miaoqing Shi, Meng Wei, Oluwatosin Alabi, Zijie Yue, and Tom Vercauteren. 2024. <a href="#">Large model driven radiology report generation with clinical quality reinforcement learning</a> . <i>Preprint</i> , arXiv:2403.06728.	
	<b>A Appendix</b>	
	<b>A.1 Supplementary Ablation Studies</b>	
	<b>Influence of the Different Reward Weight <math>\gamma</math>.</b> We analyze the effect of the reward weight $\gamma$ in Figure 5 (a). The results demonstrate that our model achieves the best performance when $\gamma = 0.5$ . In contrast, both overly large and overly small values lead to degraded outcomes. Intuitively, a large $\gamma$ overemphasizes the evidence-aware alignment reward, which can dominate the optimization signal and destabilize training. Conversely, a small $\gamma$ weakens the contribution of evidence-based alignment, providing insufficient guidance for clinically faithful grounding. Overall, a moderate $\gamma$ achieves the most favorable performance, effectively balancing alignment supervision and report generation accuracy.	
	<b>Evaluation of Different LLMs for Report Re-integration.</b> To assess the impact of different GPT-series LLMs on report re-integration, we conduct an in-depth analysis in Figure 5 (b). We evaluate several mainstream models, including GPT-4o-	

Model	Lexical Metrics				Radiology Metrics			
	BLEU-1 $\uparrow$	BLEU-4 $\uparrow$	ROUGE $\uparrow$	BERTScore $\uparrow$	RadCliQ $\downarrow$	RadGraphF1 $\uparrow$	CheXbertF1 $\uparrow$	GREEN $\uparrow$
Baseline	0.465	0.182	0.336	0.887	2.48	0.279	0.514	0.344
MedKLIP	0.485	<b>0.199</b>	0.349	0.897	<b>2.39</b>	0.301	0.521	0.392
MAVL	<b>0.487</b>	<b>0.199</b>	<b>0.352</b>	<b>0.898</b>	<b>2.39</b>	<b>0.304</b>	<b>0.522</b>	<b>0.394</b>

Table 5: Influence of Different Vision–Language Grounding Models for ESC-RL on the MIMIC-CXR test set. The best results are highlighted in bold.

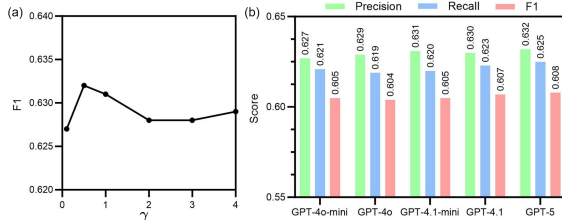


Figure 5: Ablation study. (a) The influence of the different reward weight  $\gamma$ . (b) The influence of different LLMs for report re-integration.

mini, GPT-4o, GPT-4.1-mini, GPT-4.1, and GPT-5. The results indicate that our framework consistently yields stable performance improvements across all LLMs, demonstrating the robustness of the proposed re-integration strategy. Among the evaluated models, GPT-5 achieves the best overall performance, slightly surpassing the second-best GPT-4.1 by absolute gains of 0.2%, 0.2%, and 0.1% in Precision, Recall, and F1, respectively. This advantage is consistent with the expectation that stronger LLMs exhibit better reasoning and information aggregation capabilities, leading to more accurate refinement. Therefore, we adopt GPT-5 as the default re-integration model of disease-specific observations in our framework.

**Influence of Different Vision-Language Grounding Models.** To investigate the influence of the vision–language grounding model on our framework, we conduct an ablation study by replacing MAVL (Phan et al., 2024) with MedKLIP (Wu et al., 2023), as reported in Table 5. The results show that ESC-RL consistently improves over the baseline under both grounding models, demonstrating its ability to effectively exploit grounding signals for performance gains. Moreover, the stronger grounding model (MAVL) achieves slightly better results than MedKLIP, suggesting that more accurate vision-language alignment provides higher-quality supervision for evidence-aware optimization. Importantly, ESC-RL remains superior to SOTA methods regardless of the grounding model employed,

indicating that our framework is not tied to a specific grounding backbone and generalizes well across different vision–language grounding models.

## A.2 Prompt Design for Observation Re-integration

We provide the prompt template used in the ESC-RL framework to re-integrate multiple clinical observations into a refined radiology report. The prompt guides LLMs to filter noisy or unreliable descriptions based on trustworthy disease labels, retain only evidence-consistent findings, and correct factual inconsistencies without introducing new information. By explicitly constraining the output to trusted disease evidence, the prompt facilitates self-correcting report refinement and improves clinical consistency.

```

## Role
You are an expert radiology assistant specialized in chest X-ray (CXR) interpretation and radiology report synthesis.

## Task
Your task is to Integrate multiple clinical observations with trustworthy disease labels to generate a factually consistent, and clinically aligned radiology report.

## Inputs
1. Candidate Clinical Observations: A list of multiple intermediate observations.
2. Trustworthy Disease Classes: A list of reliable disease labels.

## Task Objective
Given a set of candidate clinical observations (potentially noisy or redundant) and a predefined list of trustworthy disease classes, your task is to refine a radiology report by:
1. Filtering out any noisy or unreliable content of candidate observations that is not supported by the trustworthy disease classes;
2. Retaining only sentences that are fully consistent with the trusted disease evidence;
3. Rephrasing or correcting retained sentences when necessary to improve clinical plausibility and factual consistency, without introducing any new findings.

The final output must be a clean, self-consistent radiology report that strictly adheres to the trustworthy disease evidence.

## Refinement Rules
1. Evidence Consistency Rule
    Retain only sentences that are directly supported by the trustworthy disease classes. If multiple sentences describe the same disease with equivalent semantics, keep only the single best and most clinically appropriate sentence.
2. Exclusion Rule
    Remove any sentence that mentions diseases or findings not included in the trustworthy disease set.
3. Clinical Coherence Rule
    Ensure that the retained sentences together form a logically coherent and clinically plausible radiology report.

## Output Format
Your output must follow the structure below exactly:
<analyse>Brief reasoning on how observations were filtered and refined</analyse>
<answer>Final cleaned and corrected radiology report</answer>

```

Figure 6: The prompt template used for re-integrating multiple observations into a refined report within the ESC-RL framework using LLMs.